Journal of the Meteorological Society of Japan

EARLY ONLINE RELEASE

The DOI for this manuscript is
DOI:10.2151/jmsj.2024-029
J-STAGE Advance published date: June 11th, 2024
The final manuscript after publication will replace the preliminary version at the above DOI once it is available.

A study of zonal wavenumber 1 Rossby-gravity wave using long-term reanalysis data for the whole neutral atmosphere

Hiroto Sekido

Department of Earth and Planetary Science, The University of Tokyo, Tokyo, Japan

Kaoru Sato

Department of Earth and Planetary Science, The University of Tokyo, Tokyo, Japan

Haruka Okui

Department of Earth and Planetary Science, The University of Tokyo, Tokyo, Japan

Dai Koshin

Department of Earth and Planetary Science, The University of Tokyo, Tokyo, Japan

and

Toshihiko Hirooka

Department of Earth and Planetary Science, Kyushu university, Fukuoka, Japan

November 8, 2023

----

1) Corresponding author: Hiroto Sekido, Department of Earth and Planetary Science, The University of Tokyo, 7-3-1, Hongo, Bunkyo-ku, Tokyo 113-0033, JAPAN

Email: sekido@eps.s.u-tokyo.ac.jp

Tel: +81-3-5841-4667

Abstract

The dynamical characteristics of the zonal wavenumber 1 ($s = 1$) Rossby-gravity (RG) wave are examined using recently available reanalysis data for the whole neutral atmosphere over 16 years. An isolated peak is detected in the two-dimensional zonal wavenumber-frequency spectra that likely corresponds to the theoretically-expected $s = 1$ RG mode at heights of $z = 30, 50, 65,$ and 80 km. The wave period of the spectral peak is approximately 1.3 days, which is close to one day. The $s = 1$ RG wave is successfully extracted using a band-pass filter after removing the diurnal tide with quite large amplitudes. The $s = 1$ RG wave exhibits a characteristic seasonal variation: the geopotential height amplitudes are largest in the winter hemisphere in the stratosphere and lower mesosphere while enhancement is observed in both the winter and summer hemispheres in the upper mesosphere. Phase structures are examined in detail for a strong case. The horizontal phase structure at each height is consistent with the normal mode theory. The vertical phase structure is approximately barotropic from the lower stratosphere to the upper mesosphere at $30°N$ and $30°S$ where the amplitudes are large.

Keywords Rossby-gravity wave, normal mode, middle atmosphere

1. Introduction

The theory of free waves or normal modes of the Earth's atmosphere can be deduced from Laplace's tidal equation, which was formulated in the early nineteenth century, i.e., the classical tidal theory. According to the classical tidal theory, under the assumption of an inviscid, resting, and isothermal basic atmosphere with the boundary condition that the vertical wind velocity vanishes at the ground surface, it was shown that normal modes as external modes whose energy is trapped at the ground surface should have an equivalent depth $h = \sim 10$ km. This type of normal modes are sometimes called as Lamb modes and has a barotropic vertical structure with amplitudes proportional to $e^{\kappa z/H}$, where $\kappa \equiv R/c_{\mathrm{p}} \sim 2/7$, $R = 287\ \mathrm{JK^{-1}kg^{-1}}$ is the gas constant for dry air, c_{p} is the specific heat at constant pressure, z is the log-pressure height, and H =7 km is the scale height. Various modes with different eigenfrequencies and horizontal structures including Rossby modes, gravity modes, Kelvin modes, and Rossby-gravity modes are obtained from the Laplace's tidal equation. However, the normal modes with $h = \sim 10$ km share a common vertical structure of amplitudes, which is the same as that of the Lamb wave propagating only horizontally with the sound speed. For this reason, the normal mode is sometimes called the Lamb mode. In the present study, we refer to this type of normal mode (i.e., Lamb mode) simply as the normal mode. It is worth noting here that under realistic basic atmosphere, there is another type of normal mode, that is an internal resonant mode called Pekeris mode (Salby, 1979; 1980; Watanabe et al., 2022; Ishioka, 2023).

In the real atmosphere, several disturbances similar to the normal modes were observed in the surface pressure data (Hamilton, 1984; Hamilton and Garcia, 1986; Matsuno, 1980) and radar observation data (Hirota et al., 1983; Salby and Roper, 1980). Madden and Julian (1972) reported evidence of the zonal wavenumber $s = 1$ first symmetric Rossby normal mode by conducting a composite analysis for the surface pressure data. This mode is now known as the '5-day wave'. The discovery of the 5-day wave motivated many observational studies in the late 1970s and the 1980s, which aimed to identify other normal modes. As a result, several normal modes such as the '4-day wave', the '10-day wave', and the '16-day wave' were identified by comparing the observed and theoretical horizontal structures in the sea level pressure (Madden and Julian, 1972; 1973; Madden, 1978) and in the geopotential in the stratosphere from satellite observations (Hirota and Hirooka, 1984; Hirooka and Hirota, 1985; Rodgers, 1976). Numerical model studies (Geisler and Dickinson, 1976; Kasahara,1980; Salby, 1981a; 1981b) and observational studies have shown that the structures and wave periods of these modes are modulated by background field conditions.

Rossby-gravity (RG) modes are normal modes which have the second largest meridional structure after Kelvin modes with geopotential component having a node only at the equator. In the 1960s and the 1970s, several observational studies were conducted on wind disturbances with wave periods of approximately 2 days in the mesosphere (Leovy and Ackerman, 1973; Kingsley et al., 1978; Muller and Kingsley, 1974; Salby and Roper, 1980), which was identified as the $s = 3$ RG mode (Salby and Roper, 1980). Hereafter, the observed $s = n$ RG waves are described as RGn in the present paper. Rodgers and Prata (1981) showed that the vertical structure of the 2-day waves is consistent with the normal mode using data from the Selective Chopper Radiometer on the Nimbus 5 satellite and the Pressure Modulator Radiometer in the Nimbus 6 satellite. RG3 has large amplitudes in the summer mesosphere (e.g., Kingsley et al., 1978; McCormack et al., 2010; Pancheva et al., 2016; 2018). Using a whole atmosphere model that covers the height range from the surface to the thermosphere/ionosphere, Yasui et al. (2021) showed that waves with a wave period of ~2 days, mainly due to RG3, play a significant role in the warming of the summer mesosphere appearing several days after the warming caused by enhanced planetary wave activity in the winter stratosphere, known as interhemispheric coupling (Karlsson et al., 2009).

Observational studies showed that Rossby modes with small zonal wavenumbers tend to be dominant in the real atmosphere (e.g., Hirota and Hirooka, 1984; Hirooka and Hirota, 1985; 1989; Madden, 2007; Yamazaki et al., 2021). Among the RG modes, the 3-dimensional structures and seasonal variations of the wave activity in the middle atmosphere were examined for RG2, RG3, and RG4 (e.g., Pancheva et al., 2016; 2018). However, RG1 has not yet been examined in detail.

According to the classical normal mode theory, the $s = 1$ RG mode propagates westward with a wave period of 1.18 days. The wave period is close to that of the migrating diurnal tide (DW1), which has large amplitude in the middle atmosphere, making it difficult to extract RG1 from a short time series. The theoretical horizontal structure of $s = 1$ RG mode is shown in Fig. 1. The geopotential amplitude is largest at $34.74°\mathrm{N}$ and $34.74°\mathrm{S}$, and its phase is antisymmetric around the equator. In longitudinal regions where the geopotential component is positive (negative) in the Northern Hemisphere (NH), the horizontal wind vectors rotate clockwise (anticlockwise) over the equator and have no zonal component at the equator.

Salby and Roper (1980) analyzed data from a meteor radar in Atlanta ($34°\mathrm{N}, 84°\mathrm{W}$) over 3 years and found a dominant spectral peak at a period of 1.2 days. They suggested that this peak corresponds to the $s = 1$ RG mode. Tribbia and Madden (1988) extracted the RG1 component with a horizontal and frequency structure consistent with the normal mode theory by performing Hough function and Fourier series expansions for geopotential height at a level of $500\,\mathrm{hPa}$. They also showed that the wave amplitudes are enhanced in boreal winter and spring. Weber and Madden (1993) performed an analysis for the European Center for Medium-Range Weather Forecasts (ECMWF) operational analysis data over 10 years using a Hough function expansion and showed the presence of the $s = 1$ RG mode enhanced in the boreal winter and spring. Madden (2007) conducted EOF and spectral analysis using twice-daily 40-year reanalysis data (NCEP/NCAR Reanalysis) at a level of $300\,\mathrm{hPa}$, and showed that one of the EOF modes exhibited a horizontal structure consistent with the $s = 1$ RG mode with a wave period of approximately 1.2 days. Sakazaki and Hamilton (2020) analyzed the zonal wavenumber and frequency spectra for hourly surface pressure fluctuations from the fifth generation ECMWF atmospheric reanalysis of the global climate (ERA5) around the equator. They detected numerous discrete spectral peaks corresponding to the normal modes, including that of the $s = 1$ RG mode. They also presented horizontal structures at sea level, as well as vertical profiles of amplitudes and vertical phase structures from the surface to a level of $1\,\mathrm{hPa}$ in the equatorial region of $20°\mathrm{S}$ - $20°\mathrm{N}$. Influences of the non-uniform background of the realistic atmosphere on the $s = 1$ RG mode were theoretically investigated by Salby (1981b). His results indicated that the overall structure and wave period were slightly different from, but essentially similar to, those of the classical normal mode theory. This similarity is attributed to its significantly faster phase speed compared to the background zonal winds. Nevertheless, the characteristics of RG1, including phase structure and seasonal variations in the real middle atmosphere, remain unknown.

The analysis of RG1 requires a sufficiently high-frequency resolution to distinguish it from DW1. Data with sufficiently long time period and coverage spanning the entire middle atmosphere for such an analysis have been limited until recent years. The recently generated reanalysis dataset using the Japanese Atmospheric General Circulation Model for Upper Atmosphere Research-Data Assimilation System (JAGUAR-DAS; Koshin et al., 2020; 2022) satisfies these requirements. Thus, in the present study, we examine RG1 characteristics in the middle atmosphere utilizing JAGUAR-DAS reanalysis dataset. The data and methodology of the analysis are described in Section 2. Section 3 presents the wave characteristics of RG1, while Section 4 discusses the seasonal variation of RG1 and compares it with that of RG3 reported in previous studies. Conclusions are given in Section 5.

Fig. 1

2. Data and Analysis Method

2.1. JAGUAR-DAS reanalysis data

We used the reanalysis dataset over 16 years from September 2004 to August 2020 covering the whole neutral atmosphere from the data assimilation system called JAGUAR-DAS(Koshin et al., 2020; 2022). The four-Dimensional Local Ensemble Transform Kalman Filter (4D-LETKF; Miyoshi and Yamane, 2007) was employed as a data assimilation method for JAGUAR-DAS. The forecast model, called JAGUAR (Watanabe and Miyahara, 2009), has a T42 horizontal resolution (a latitude interval of $2.8125°$) and 124 vertical layers from the surface to a height of $z =$ ~150 km. The vertical grid spacing is about $1\ \mathrm{km}$. The assimilated observations are PREPBUFR provided by the National Centers for Environmental Prediction (NCEP), temperatures from the Microwave Limb Sounder (MLS v4.2; Livesey et al., 2020) aboard NASA's Aura satellite and from the Sounding of the Atmosphere using Broadband Emission of Radiation (SABER v2.0; Remsberg et al., 2008) aboard the Thermosphere Ionosphere Mesosphere Energetic and Dynamics (TIMED) satellite, and brightness temperatures from the Defense Meteorological Satellite Program (DMSP) Special Sensor Microwave Imager/Sounder (SSMIS; Swadley et al., 2008). The NCEP PREPBUFR includes temperature, wind, humidity, and surface pressure data from radiosondes, aircrafts, wind profilers, and satellites, mainly covering the troposphere and the lower stratosphere. Temperature data from the Aura MLS and TIMED SABER are available for altitude ranges of $z = \sim 16\text{-}90$ km with ~ 2 km intervals and of $\sim 15\text{-}110$ km with ~ 1 km intervals, respectively. Measurements by the SSMIS cover an altitude range of $z = \sim 30\text{-}90$ km. The 4D-LETKF has a relatively low computational cost, making it possible to produce a long-period reanalysis with realistic computing resources. In this study, we used 6-hourly data for 16 years from September 2004 to August 2020 covering the log-pressure height range of 10 km (~240 hPa) to 100 km (~6.2$\times 10^{-4}$ hPa) with a scale height of 7 km, that is, the whole middle atmosphere.

2.2. 2-dimensinal Spectral analysis

A 2-dimensional (2-D) spectral analysis on zonal wavenumbers and frequencies for geopotential height (GPH) fluctuations is performed to confirm the presence of RG1 for 30°S near the GPH amplitude maximum predicted by the classical normal mode theory. The analyzed altitudes are 30, 50, 65, and 80 km, respectively, corresponding to the middle stratosphere, near the stratopause, in the middle mesosphere, and in the upper mesosphere. The 16-year time period of the data results in a high frequency resolution of $\Delta\omega = \sim 1.1 \times 10^{-3}$ rad day^{-1}.

2.3. Method of the extraction of RG1

The westward propagating $s = 1$ components of the GPH fluctuations at 30°S are extracted, and the frequency spectra for the components are averaged over $z = 45\text{-}55$ km. The chosen altitude range encompasses altitudes where various normal modes have previously been identified in the middle atmosphere (e.g., Hirota and Hirooka, 1984; Hirooka and Hirota, 1985). The black curve in

Fig. 2 shows the result. An isolated spectral peak corresponding to RG1 is clearly visible, adjacent to a quite strong peak of DW1 at the 1-day period. Note that frequency resolution is inversely proportional to the length of the time series. These two closely spaced spectral peaks can be distinguished due to the utilization of a long time series spanning over 16 years.

Because of the close proximity of the wave periods of RG1 and DW1, and the significant DW1 spectral density, including its lower portion, its potential contamination into the passband of a filter designed to extract the RG1 component is considered substantial. Thus, the DW1 component is removed from the time series of the westward $s = 1$ fluctuations beforehand using. The following procedure: the DW1 component is obtained as the running mean of the westward $s = 1$ fluctuation time series for each local time at each grid point (Yasui et al., 2018). In order to properly represent the seasonal variation of DW1, the length of the running mean is taken as 20 days. The DW1 time series after applying a 20-day running mean is subtracted from the westward $s = 1$ fluctuation time series. The red curve in Fig. 2 shows the frequency power spectrum after removing the DW1 component. The significant spectral peak of DW1 and its floor part become weaker, although the red curve almost overlaps the black curve in the wave period band far from the 1-day period. The frequency spectra shown in Fig. 2 were smoothed with a 5-point running mean, and hence the degree of freedom is 10. This implies that the effective frequency resolution of the spectrum is $\Delta\omega_{\mathrm{eff}} = \sim 5.4 \times 10^{-3}\ \mathrm{rad\ day}^{-1}$, which is sufficient to separate the two spectral peaks. The spectral peak of RG1 in Fig. 2 is located at a wave period of 1.3 days. This wave period differs slightly from the theoretically derived wave periods of RG1, that is 1.18 days in the classical theory and 1.24–1.29 days for a realistic but ideal background field obtained by Salby (1981b). This difference is likely due to the modulation of the wave period by the real middle atmosphere conditions. This wave period is also slightly different from previous observational studies, which reported a period of ~1.2 days in the troposphere (e.g., Madden, 2007) and near the mesopause (Salby and Roper, 1980). This difference can be attributed to the difference in the exact altitude region analyzed and in the duration of the time series.

Fig. 2

Last, the Ormsby band-pass filter (Ormsby, 1961) is applied to the westward $s = 1$ fluctuation time series from which the DW1 component have been removed, and the RG1 component is extracted. Note that this filter had been often used to separate normal mode components in the previous studies (Hirota and Hirooka, 1984; Hirooka and Hirota, 1985). The cut-off frequencies, $2\pi/1.11$ rad day^{-1} and $2\pi/1.58$ rad day^{-1}, were determined based on the observed spectral peak (Fig. 3), as indicated by the green dashed lines in Fig. 2.

Fig. 3

3. Results

3.1 The results of spectral analysis

The 2-D power spectra for the original GPH fluctuations, which include DW1, at $30°$S are shown for $z = 30, 50, 65,$ and 80 km in Fig. 4 using the data spanning 16 years. A 5-point running mean is made for the frequency direction, resulting in an effective frequency resolution of $\Delta\omega_{\text{eff}} = \sim 5.4 \times 10^{-3}$ rad day^{-1}. In each panel, the black curve represents the dispersion curve of the RG normal modes, and the black circle shows the theoretical location of the westward $s = 1$ RG mode.

At all altitudes, isolated spectral peaks are observed around the black circles. Additionally, several isolated spectral peaks are observed on the dispersion curve of the RG normal modes. Note that these peaks are properly separated considering the sufficiently fine $\Delta\omega_{\text{eff}}$. The spectral peaks corresponding to quasi-2-day waves with westward $s = 2$ and $s = 3$ are significant. It is worth noting that distinct spectral peaks are also observed corresponding to the $s = 0$ and eastward $s = 1$ RG modes. Note that the eastward modes on the dispersion curve are generally called the gravity modes. However, in this paper, the eastward modes are also referred to as the RG modes for convenience. At a frequency of $2\pi/1$ rad day^{-1}, large spectral densities are distributed over a wide range of the zonal wavenumber, owing to diurnal tides. In particular, the westward-propagating $s = 1$ spectral peak is predominant, corresponding to DW1.

Fig. 4

3.2 The structure of RG1

Time-latitude sections of the climatology of the RG1 GPH amplitude are shown for $z = 30, 50, 65,$ and 80 km in Fig. 5. A15-day running mean was applied. Hereafter, unless otherwise noted, the results are shown using the RG1 component obtained by the method in Section 2.3. For all heights over the whole year, the RG1 GPH amplitude is maximized near $30°$N and $30°$S, while the amplitude is minimized near the equator, which is consistent with the theoretical latitudinal structure of the $s = 1$ RG mode. The seasonal variation of the GPH amplitude near $30°$N and $30°$S is similar at $z = 30, 50,$ and 65 km, with relatively large values in the winter hemisphere and small values in the summer hemisphere.

In contrast, at $z = 80$ km, the GPH amplitude near $30°$N and $30°$S is large in both solstitial seasons, especially in boreal winter. The latitudinal structure of the GPH amplitude is almost symmetric around the equator. The GPH amplitude is ~ 34 m in the NH and ~ 32 m in the Southern Hemisphere (SH) in boreal winter, while in austral winter, the amplitude is ~ 22 m in the NH and ~ 25 m in the SH. In the equinoctial seasons, the amplitude is weak but ranges from 13 to 18 m.

In the seasonal variation, high equatorial symmetry of the latitudinal distribution of the RG1 GPH amplitude near $30°$N and $30°$S at $z = 50$ km is observed during March to April and September to October, while it is low during December to January and June to July. Equatorial symmetry during the solstitial seasons increases with height.

At each height, the GPH amplitude is also maximized in the winter high latitudes of both the NH and SH. However, the coherence between the maximum of RG1 GPH amplitude at the winter high latitudes and that at the $30°$S is low (not shown). This fact suggests that the high latitude maximum is not due to RG1, which is consistent with the theory of the $s = 1$ RG normal mode. Instead, the maximum at high latitudes can be attributed to the disturbances in a wide range of wave periods associated with significant large-scale variability, such as stratospheric sudden warmings. Therefore the disturbances corresponding to the high-latitude maximum are not further examined in this study.

Fig. 5

Time-latitude sections of the RG1 GPH amplitude over 16 years are shown for $z = 30, 50, 65,$ and 80 km in Fig. 6. Note that a 15-day running mean is not applied for Fig. 6. The characteristics observed in the climatology (Fig. 5), with two maxima near $30°$N and $30°$S and a minimum near the equator are commonly observed in all years albeit with nonnegligible interannual variation.

At $z = 80$ km, it is noteworthy that large GPH amplitudes extend over both hemispheres almost every boreal winter. In several cases, such as January 2006, January 2007, December 2009, and January 2015, the RG1 GPH amplitude is remarkably large, exceeding 80 m at $z = 80$ km in both hemispheres. In the case of December 2009, the GPH amplitude is quite large not only at z =80 km, but also z =50 and 65 km, although the magnitude is slightly larger in the NH than that in the SH. In seasons other than boreal winter, large amplitudes extending over both hemispheres are observed in August 2010, July 2014, and September 2019. Particularly in September 2019, when a minor stratospheric warming occurred in the SH, large amplitude regions are clearly observed in the low and middle latitudes in both hemispheres at $z = 50, 65,$ and 80 km.

Fig. 6

Figure 7 shows latitude-height sections of the climatology of the RG1 GPH amplitude for the solstitial seasons (December to January and June to July) and equinoctial seasons (March to April and September to October). Note that the GPH amplitude was weighted by the inverse of the vertical profile of the Lamb mode amplitude, $\sqrt{\overline{\mathrm{GPH}'^2}} \times e^{-\kappa z/H}$; the result is hereafter referred to as the normalized GPH amplitude. With this weighting, for the Lamb mode in the classical theory, its amplitude would be constant with altitude. This procedure helps to highlight regions where the observed RG1 deviates from the theoretical profile. The four seasons were determined considering the meridional symmetry of the RG1 GPH amplitude observed in Fig. 5. It is seen that the normalized GPH amplitude is maximized near $30°$N and $30°$S and minimized near the equator at most heights for all seasons. This feature is again consistent with the latitudinal structure of the $s = 1$ RG mode.

In the equinoctial seasons, the latitudinal distribution of the normalized GPH amplitude is roughly symmetric around the equator at all heights, and the GPH amplitudes are maximized at the

Fig. 7

lower mesosphere. In the solstitial seasons, the normalized GPH amplitude in the winter hemisphere is larger in the upper stratosphere and the middle mesosphere than that in the summer hemisphere. This feature suggests the presence of wave sources in the winter hemisphere. In contrast, near the mesopause around z =90 km, the normalized GPH amplitude is larger in summer hemisphere than in the winter hemisphere. Comparing the features across different seasons, it becomes evident that the normalized GPH amplitude is greater in the solstitial seasons in the middle and upper mesosphere compared to the equinoctial seasons, with the highest values observed in most latitudes in the boreal winter. In the stratosphere and the lower mesosphere, the normalized GPH amplitude is the largest in the winter hemisphere, moderate in the spring and autumn hemispheres, and smallest in the summer hemisphere.

A time-height section of the normalized GPH amplitude at 30°N is shown for the 16 years in Fig. 8. In the mesosphere, the seasonal variation of the normalized GPH amplitude is clear for all years, i.e., large in winter and small in summer. In addition, strong cases with large amplitude over a wide altitude range are occasionally observed. For example, in December 2009, the normalized GPH amplitude is large for a wide range of altitudes from 40 to 100 km, which is consistent with the features observed in the time-latitude section of the GPH amplitude in Fig. 6. Thus, a more detailed analysis of the wave structure is undertaken for this particular case.

Fig. 8

Figure 9 represents a time-height section of the normalized GPH amplitude and zonal mean zonal wind at 30°N for the time period of November 20 through December 15, 2009. The normalized GPH amplitude starts to increase from November 26 in the altitude range of z =35-65 km. The normalized GPH amplitude reaches its maximum at z =80 km on December 5. The date of maximum normalized GPH amplitude shift to later date with increasing altitude: at $z = 50$ km, the maximum is reached on December 4, at $z = 80$ km on December 5, and at $z = 100$ km on December 9, which indicates upward energy penetration. Note that owing to the relatively poor time domain resolution of the band-pass filter (Fig. 3a), the normalized GPH amplitude peak is not sharp in time. Nevertheless, the upward penetration remains evident.

Fig. 9

The time evolution of the strong RG1 case is examined in the latitude-height section. Fig. 10 presents the normalized RG1 GPH amplitude depicted for every 3 days from 00UTC on November 28 to 00UTC on December 7, 2009. At 00UTC on November 28, 2009, the normalized GPH amplitude is larger in the NH than in the SH. In the altitude range with particularly large GPH amplitude near $30°S$ and $30°N$, such as z =45–100 km at 00UTC on December 7, 2009, the GPH amplitude is minimized near the equator, which is consistent with the theoretical RG1 structure. In the mesosphere and lower thermosphere, the GPH amplitude increases with time. Fig. 10

To examine the horizontal phase structure and its time evolution, horizontal maps of the RG1 GPH component along with the RG1 horizontal wind vectors are shown for $z = 80$ km every 6 hours from 00UTC on December 4 to 06 UTC on December 5, 2009 in Fig. 11. At 00UTC on December 4, the GPH component has positive maxima at $(90°E, 25°N)$ and $(90°W, 30°S)$, and negative maxima at $(90°W, 25°N)$ and $(90°E, 30°S)$. The amplitude is also maximized in winter high latitudes, but this maximum is likely not attributed to the normal mode as previously described.

The latitudinal phase structure of the GPH component exhibits approximately antisymmetry with respect to the equator at latitudes below around $60°N$ and $60°S$. The meridional phase differences are minimal within each hemisphere. The maximum amplitude of the GPH component at $30°N/30°S$ is about 80 m, although it is slightly larger in the SH than in the NH. The horizontal wind vectors are meridional near the equator. In the longitudinal region where the GPH component is positive in the NH and negative in the SH, the horizontal winds blow clockwise over both hemispheres. For an opposite phase region, the direction of the horizontal winds also reverses, Fig. 11 conversely. This phase structure, including the relation between the GPH and horizontal wind components, is consistent with the theory of the $s = 1$ RG mode (Fig. 1). As observed in Fig. 11, the RG1 propagates westward over the globe with a wave period of ~1.25 days. Similarly, the horizontal phase structure at other heights is consistent with the RG mode theory (not shown).

Finally, to examine the vertical phase structure, the longitude-height sections of a normalized GPH component, i.e., $\mathrm{GPH}' \times e^{-\kappa z/H}$, are shown in Fig. 12 for $30°N$ and $30°S$ at 00UTC on

December 4, 2009. The phases tilt slightly westward with height. However, considering the extensive height range over 90 km displayed in Fig. 12, the phase structure can be regarded as quasi-barotropic. Additionally, the phases differ by about 180° between 30°N and 30°S, which is also consistent with the $s = 1$ RG mode theory. The slight westward phase tilt with height is a common characteristic of westward free waves observed as normal modes (e.g., Hirota and Hirooka, 1984; Hirooka and Hirota, 1985; Sakazaki and Hamilton, 2020) and is attributable to thermal relaxation (e.g., Salby, 1981b). The westward phase tilt with height implies that this westward propagating wave transports energy upward.

Fig. 12

Other strong cases are observed in January 2006, January 2007, January 2015, and September 2019 (see Figs. 6 and 8). These cases were also analyzed using the same method. In each case, the GPH amplitude begins to increase in the middle atmosphere and its maxima shift upward with time. The horizontal structure analyzed for the height where the normalized GPH amplitude is largest was also consistent with the classical theory. The westward phase tilt with height is commonly observed for the four cases, albeit slightly larger than observed in December 2009. Additionally, the GPH amplitude in the stratosphere is consistently greater in the winter hemisphere than in the summer one. It is also worth noting that large normalized GPH amplitudes are commonly observed in winter high latitudes for all strong RG1 cases, including December 2009 (see Fig. 6 as well), suggesting a connection with the presence of the RG1 wave.

4. Discussion

Using numerical experiments, Salby (1981b) and Salby and Callaghan (2001) demonstrated theoretically that the $s = 1$ RG mode is amplified more strongly in the solstitial background conditions than in the equinoctial ones. The seasonal variation characteristics of RG1, such as its dominance during solstitial seasons in the upper mesosphere, revealed by the present study using the JAGUAR-DAS reanalysis dataset, are consistent with their studies.

Previous observational studies showed that RG3 exhibits significantly large amplitudes only in the summer mesosphere (e.g., Kingsley et al., 1978; Pancheva et al., 2016; 2018). This seasonal variation of RG3 is distinct from that of RG1, which, as revealed by the present study, has large amplitudes in both the summer and winter mesospheres. There are several proposed mechanisms for the enhancement of RG3 in the summer mesosphere; Salby (1981b) suggested that the enhancement of RG3 specifically in the summer mesosphere is attributed to the significant difference in the background wind field between the two hemispheres. Plumb (1983) and Pfister (1985) discussed the role of the baroclinic instability resulting from the summer easterly jet in the mesosphere as a factor contributing to the large RG3 amplitudes. Dickinson (1973) showed that the region of negative meridional gradient of the potential vorticity can serve as a source of waves having their critical line in that region. Salby and Callaghan (2001) suggested based on the analysis of the EP flux divergence that the presence of critical lines for RG3 in the regions with negative meridional gradient of the potential vorticity related to the summer easterly jet is important.

While the RG3 amplitudes are large in the summer hemisphere, the RG1 amplitudes are enhanced in both the summer and winter hemispheres. The zonal phase speed of RG1 is so fast that the critical line does not exist even in the easterly jet region in the summer hemisphere. There are the regions with negative meridional gradient of the potential vorticity in the summer mesosphere form November to December 2009, when strong RG1 was observed. However, the significant EP flux divergence due to RG1, was not observed (not shown). Thus, the background fields for the RG1 do not satisfy the preferable amplification condition proposed for the RG3 enhancement in the summer mesosphere.

As shown in Fig. 7, the normalized RG1 GPH amplitude is maximized below the tropopause. The GPH amplitude is minimized near the equator and tends to be larger at higher latitudes, which is not consistent with the theoretical structure of RG1. However, the squared coherence with respect to the time series at 30°S and z =10 km is large at low and middle latitudes in the NH (not shown), suggesting that the GPH amplitude includes the RG1 component at low and middle latitudes, although it also includes other wave components at high latitudes. It is possible that the energy source of RG1 is in the troposphere, such as the diabatic heating associated with tropical convection (Salby and Garcia, 1987; Miyoshi and Hirooka, 1999). In addition, the normalized GPH amplitude exhibit significant peaks in the middle atmosphere in the climatology (Fig. 7), as well as in strong cases, including that in December 2009 (Figs. 9, 11, and 12). This fact suggests the presence of energy sources for RG1 in the middle atmosphere. A plausible candidate of such sources is the disturbances associated with large-scale prominent phenomena in the middle atmosphere such as stratospheric sudden warmings in the winter stratosphere. The maximum of the normalized GPH amplitude in the winter polar region shown in Figs 6, 7, and 10 supports this influence. On the other hand, Salby (1979) showed that the vertical structure of the Lamb mode is slightly deformed for the realistic vertical temperature profile. According to his study, the Lamb mode amplitude is minimized at $z =$~18 km and ~110 km and maximized at $z =$~45 km. The characteristics of normalized RG1 GPH amplitude at $30°\mathrm{N}$ and $30°\mathrm{S}$ shown in Fig. 7b and 7c are similar to those shown by Salby (1979). Our result may include deformation of the normal mode structure due to the effect of real atmospheric fields. Further studies are needed to elucidate the detailed mechanisms of wave forcing, which are beyond the scope of the present study.

5. Conclusions

The characteristics of RG1 have been examined using the JAGUAR-DAS reanalysis data over a long time period of 16 years, covering the entire neutral atmosphere up to the lower thermosphere. Two-dimensional spectral analysis for zonal wavenumbers and frequencies was performed for the GPH fluctuations for $30°\mathrm{S}$ and heights of $z = 30, 50, 65$ and 80 km. As a result, an isolated spectral peak corresponding to the $s = 1$ RG mode could be identified at each height. The distinction between the RG1 peak and the strong DW1 peak, which are located at the same zonal wavenumber and similar frequencies, was possible due to the long time series, which provided sufficiently high frequency resolution. The RG1 component was adequately extracted by removing the DW1 component before applying a band-pass filter.

The climatological features of RG1 in the middle atmosphere were examined. The GPH amplitudes are maximized around 30°N and 30°S, and minimized around the equator. This agrees well with a common theoretical property of RG normal modes. The RG1 GPH amplitude exhibits a characteristic seasonal variation. In the solstitial seasons, the GPH amplitude is larger in the winter hemisphere than in the summer hemisphere in the stratosphere and lower mesosphere, while it is comparable between the two hemispheres in the upper mesosphere. The normalized GPH amplitude is large in the upper mesosphere in the winter hemisphere, while it is large in the lower and middle mesosphere in the summer hemisphere. In the equinoctial seasons, the GPH amplitude is distributed approximately symmetrically around the equator at all heights. The normalized GPH amplitude is maximized in the lower mesosphere.

A case study was performed for December 2009, which marked the period with largest RG1 GPH amplitude at $z = 80$ km. In the upper mesosphere, the horizontal structures reveal that the GPH component is approximately 180° out of phase between the NH and the SH. Additionally, the horizontal winds exhibit rotation across both hemispheres, with a zero zonal wind component on the equator. The vertical phase structures are nearly barotropic at 30°N and 30°S in the height region of 10-90 km. The horizontal and vertical phase structures are consistent with the $s = 1$ RG normal mode theory. The normalized GPH amplitude is large above the middle stratosphere, suggesting an energy source in the middle stratosphere. Strong wave disturbances observed in the stratosphere in the winter high latitudes is one of the plausible candidates of such source.

Previous theoretical study showed that the vertical structure of the Lamb mode in the real atmosphere differs from that in the resting isothermal atmosphere. The climatological characteristics of the normalized RG1 GPH amplitude in the equinoctial seasons, such as minima and maxima at z =~20 km and ~60 km, are similar to the characteristics of the deformation of the Lamb mode structure obtained theoretically. However, the normalized GPH amplitude maxima near the mesopause and the characteristics in the solstitial seasons cannot be explained by the deformation alone. Previous studies have indicated that normal modes are mainly excited in the troposphere. The maximum of the normalized RG1 GPH amplitude below the tropopause obtained in the present study may be related to this suggestion. Additionally, previous studies have suggested that the barotropic/baroclinic instability in the mesosphere is also related to the amplification of certain normal modes, such as RG3 which has critical lines in the mesosphere. At first glance, this seems consistent with our result that the normalized RG1 GPH amplitude is maximized vertically also in the middle atmosphere. However, this is not the case because RG1 has such a fast phase speed that it does not have critical lines in the middle atmosphere in any season. Further studies on the excitation mechanism of RG1 in the middle atmosphere and its role in the middle atmosphere dynamics are crucial.

Data Availability Statement

The JAGUAR-DAS data used in this study are available at https://pansy.eps.s.u-tokyo.ac.jp/archive_data/Sekido_etal_2023/.

Acknowledgments

We thank two anonymous reviewers for their constructive comments. This work was supported by JSPS KAKENHI Grant Numbers JP22H00169 (KS) and JP20H01973 (TH). All figures in this paper were created using the Dennou Club Library (DCL).

References

Andrews, D. G., J. R. Holton, and C. B. Leovy, 1987: Middle atmosphere dynamics. *Academic Press*, 489 pp.

Dickinson, R. E. (1973). Baroclinic instability of an unbounded zonal shear flow in a compressible atmosphere. *Journal of the Atmospheric Sciences*, **30**(8), 1520-1527, https://doi.org/10.1175/1520-0469(1973)030%3C1520:BIOAUZ%3E2.0.CO;2

Geisler, J. E. and Dickinson, R. E. (1976). The five-day wave on a sphere with realistic zonal winds. *Journal of the Atmospheric Sciences*, **33**(4), 632–641, https://doi.org/10.1175/1520-0469(1976)033%3C0632:TFDWOA%3E2.0.CO;2

Hamilton, K (1984). Evidence for normal mode Kelvin wave in the atmosphere, *Journal of Meteorological Society of Japan*, **62**(2), 308–311. https://doi.org/10.2151/jmsj1965.62.2_308

Hamilton, K. and Garcia, R. R. (1986). Theory and observations of the short-period normal mode oscillations of the atmosphere, *Journal of Geophysical Research*, **91**(11), 11867–11875. https://doi.org/10.1029/JD091iD11p11867

Hirooka, T. & Hirota, I (1985). Normal mode Rossby waves observed in the upper stratosphere. Part II: second antisymmetric and symmetric modes of zonal wavenumber 1 and 2. *Journal of the Atmospheric Science*, **42**(6), 536–548. https://doi.org/10.1175/1520-0469(1985)042%3C0536:NMRWOI%3E2.0.CO;2

Hirooka, T. & Hirota, I. (1989). Further evidence of normal mode Rossby waves. *Pure Applied Geophysics*, **130**, 277–289. https://doi.org/10.1007/978-3-0348-5825-0_10

Hirota, I. & Hirooka, T. (1984). Normal mode Rossby waves observed in the upper stratosphere. Part I: first symmetric modes of zonal wavenumbers 1 and 2. *Journal of the Atmospheric Science*, **41**(8), 1253–1267. https://doi.org/10.1175/1520-0469(1984)041%3C1253:NMRWOI%3E2.0.CO;2

Hirota, I., Maekawa, S., Fukao, K., Fukuyama, M., Sulzer, M. P., Fellous, J. L., Tsuda, T., and Kato, S. (1983). Fifteen-day observation of mesospheric and lower thermospheric motions with the aid of the Arecibo UHF radar, *Journal of Geophysical Research*, **88**(11), 6835–6842.https://doi.org/10.1029/JC088iC11p06835

Ishioka, K. (2023). What is the equivalent depth of the Pekeris mode? *Journal of Meteorological Society of Japan*, **101**(2), 139-148, https://doi.org/10.2151/jmsj.2023–008

Kasahara, A. (1980). Effect of zonal flow on the free oscillations of a barotropic atmosphere. *Journal* *of the Atmospheric Sciences*, **37**(5), 917–929. https://doi.org/10.1175/1520-0469(1980)037%3C0917:EOZFOT%3E2.0.CO;2

Karlsson, B., McLandress, C., and Shepherd, T. G. (2009). Inter-hemispheric mesospheric coupling in a comprehensive middle atmosphere model. *Journal of Atmospheric and Solar-Terrestrial Physics*, **71**(3–4), 518–530. https://doi.org/10.1016/j.jastp.2008.08.006

Kingsley, S., Muller, H., Nelson, L., and Scholefield. (1978). Meteor winds over Sheffield (53°N, 2°W). *Journal of Atmospheric and Terrestrial Physics*, **40**(8), 917–922. https://doi.org/10.1016/0021-9169(78)90143-5

Koshin, D., Sato, K., Kohma, M., and Watanabe, S. (2022). An update on the 4D-LETKF data assimilation system for the whole neutral atmosphere. *Geoscientific Model Development*, **15**(5), 2293–2307. https://doi.org/10.5194/gmd-15-2293-2022

Koshin, D., Sato, K., Miyazaki, K., & Watanabe, S. (2020). An ensemble Kalman filter data assimilation system for the whole neutral atmosphere. *Geoscientific Model Development*, **13**(7), 3145–3177. https://doi.org/10.5194/gmd%26%23x02212%3B13-3145-2020

Leovy, C. B. and Ackerman, T., (1973). Evidence for high-frequency synoptic disturbances near the stratopause. *Journal of the Atmospheric Sciences*, **30**(5), 940–942. https://doi.org/10.1175/1520-0469(1973)030%3C0940:EFHFSD%3E2.0.CO;2

Livesey, N. J., Read, W. G., Wagner, P. A., Froidevaux, L., Lambert, A., Manney. G. L., Millán Valle, L. F., Pumphrey, H. C., Santee, M. L., Schwartz, M. J., Wang, S., Fuller, R. A., Jarnot, R. F., Knosp, B. W., Martinez, E., and Lay, R. R. (2020). Aura Microwave Limb Sounder (MLS) Version 4.2× Level 2 and 3 data quality and description document, https://mls.jpl.nasa.gov/data/ v4-2_data_quality_document.pdf, last access

Madden, R. A. (1978). Further evidence of traveling planetary waves. *Journal of the Atmospheric Sciences*, **35**(9), 1605–1618. https://doi.org/10.1175/1520-0469(1978)035%3C1605:FEOTPW%3E2.0.CO;2

Madden, R. A. (2007). Large-scale, free Rossby waves in the atmosphere-An update. *Tellus*, **59A**, 571–590. https://doi.org/10.1111/j.1600-0870.2007.00257.x

Madden, R. A. & Julian, P. (1972). Further evidence of global-scale, 5-Day pressure waves. *Journal of the Atmospheric Sciences*, **29**(8), 1464–1469. https://doi.org/10.1175/1520-0469(1972)029%3C1464:FEOGSD%3E2.0.CO;2

Madden, R. A. and Julian, P. (1973). Reply. *Journal of the Atmospheric Sciences*, **30**(5), 935–940. https://doi.org/10.1175/1520-0469(1973)030%3C0935:R%3E2.0.CO;2

Matsuno, T. (1980). A trial of search for minor components of lunar tides and short period oscillations of the atmosphere in surface pressure data. *Journal of Meteorological Society of Japan*, **58**(4), 281–285. https://doi.org/10.2151/jmsj1965.58.4_281

McCormack, J. P., Eckermann, S. D., Hoppel, K. W., and Vincent, R. A. (2010). Amplification of the quasi-two day wave through nonlinear interaction with the migrating diurnal tide. *Geophysical Research Letters*, **37**, L16810. https://doi.org/10.1029/2010GL043906

Miyoshi, Y. and Hirooka, T. (1999). A numerical experiment of excitation of the 5-day wave by a GCM. *Journal of the Atmospheric Sciences*, **56**(11), 1698–1707. https://doi.org/10.1175/1520-0469(1999)056%3C1698:ANEOEO%3E2.0.CO;2

Miyoshi, Y. and Yamane, S. (2007). Local ensemble transform Kalman filtering with an AGCM at a T159/L48 resolution. *Monthly Weather Review*, **135**(11), 3841–3861. https://doi.org/10.1175/2007MWR1873.1

Muller, H. and Kingsley, S. (1974). On the scale sizes of wind systems in the meteor zone. *Journal of Atmospheric and Terrestrial Physics*, **36**(11), 1851–1861. https://doi.org/10.1016/0021-9169(74)90171-8

Ormsby, J. F. A. (1961). Design of numerical filters with applications to missile data processing. *Journal of Association for Computing Machinery*, **8**(3), 440–466. https://doi.org/10.1145/321075.321087

Pancheva, D., Mukhtarov, P., and Siskind, D. E. (2018). Climatology of the quasi-2-day waves observed in the MLS/Aura measurements (2005-2014). *Journal of Atmospheric and Solar-Terrestrial Physics*, **171**, 210–224. https://doi.org/10.1016/j.jastp.2017.05.002

Pancheva, D., Mukhtarov, P., Siskind, D. E., and Smith. A. K. (2016). Global distribution and variability of quasi 2day waves based on the NOGAPS-ALPHA reanalysis model. *Journal of Geophysical Research: Space Physics*, **121**(11), 422–449. https://doi.org/10.1002/2016JA023381

Pfister, L. (1985). Baroclinic instability of easterly jets with applications to the summer mesosphere. *Journal of the Atmospheric Science*, **42**(4), 313–330. https://doi.org/10.1175/1520-0469(1985)042%3C0313:BIOEJW%3E2.0.CO;2

Plumb, A. (1983). Baroclinic instability of the summer mesosphere: A mechanism for the quasi-two-day wave? *Journal of the Atmospheric Science*, **40**(1), 220–262. https://doi.org/10.1175/1520-0469(1983)040%3C0262:BIOTSM%3E2.0.CO;2

Remsberg, E. E., Marshall, B. T., Garcia-Comas, M., Krueger, D., Lingenfelser, G. S., Martin-Torres, J., Mlynczak, M. G., Russell III, J. M., Smith, A. K., Zhao, Y., Brown, C., Gordley, L. L., Lopez-Gonzalez, M., Lopez-Puertas, M., She, C.-Y., Taylor, M. J., and Thompson, R. E. (2008). Assessment of the quality of the Version 1.07 temperature-versus-pressure profiles of the middle atmosphere from TIMED/SABER. *Journal of Geophysical Research: Space Physics.*, **113**, D17101. https://doi.org/10.1029/2008JD010013

Rodgers, C. D. (1976). Evidence for the five-day wave in the upper stratosphere. *Journal of the Atmospheric Sciences*, **33**(4), 710–711. https://doi.org/10.1175/1520-0469(1976)033%3C0710:EFTFDW%3E2.0.CO;2

Rogers, C. and Prata, A. (1981). Evidence for a traveling two-day wave in the middle atmosphere. *Journal of Geophysical Research*, **86**(C10), 9661–9664. https://doi.org/10.1029/JC086iC10p09661

Sakazaki, T. and Hamilton, K. (2020). An array of ringing global free modes discovered in tropical surface pressure data. *Journal of the Atmospheric Sciences*, **77**(7), 2519–2539. https://doi.org/10.1175/JAS-D-20-0053.1

Salby, M. L. (1979). On the solution of the homogeneous vertical structure problem for long-period oscillations. *Journal of the Atmospheric Sciences*, **36**(12), 2350–2359. https://doi.org/10.1175/1520-0469(1979)036%3C2350:OTSOTH%3E2.0.CO;2

Salby, M. L. (1980). The influence of realistic dissipation on planetary normal structures. *Journal of the Atmospheric Sciences*, **37**, 2186–2199. https://doi.org/10.1175/1520-0469(1980)037%3C2186:TIORDO%3E2.0.CO;2

Salby, M. L. (1981a). Rossby normal modes in nonuniform background configurations I, Simple fields. *Journal of the Atmospheric Sciences*, **38**(9), 1803–1826. https://doi.org/10.1175/1520-0469(1981)038%3C1803:RNMINB%3E2.0.CO;2

Salby, M. L. (1981b). Rossby normal modes in nonuniform background configurations. Part II: equinox and solstice conditions. *Journal of the Atmospheric Sciences*, **38**(9), 1827–1840. https://doi.org/10.1175/1520-0469(1981)038%3C1827:RNMINB%3E2.0.CO;2

Salby, M. L. & Callaghan, P. F. (2001). Seasonal amplification of the 2-day wave: relationship between normal mode and instability. *Journal of the Atmospheric Science*, **58**(14), 1858–1869. https://doi.org/10.1175/1520-0469(2001)058%3C1858:SAOTDW%3E2.0.CO;2

Salby, M. L. & R. R. Garcia. (1987). Transient response to localized episodic heating in the tropics. Part I: Excitation and short-time near-field behavior. *Journal of the Atmospheric Sciences*, **44**(2), 458–498. https://doi.org/10.1175/1520-0469(1987)044%3C0458:TRTLEH%3E2.0.CO;2

Salby, M. L. and Roper, R. G. (1980). Long-period oscillations in the meteor region. *Journal of the Atmospheric Sciences*, **37**(1), 237–244. https://doi.org/10.1175/1520-0469(1980)037%3C0237:LPOITM%3E2.0.CO;2

SSMIS: SSMIS Unified Pre-Procesed TDRs BUFR, SSMIS [data set], https://www.avl.class.noaa.gov/saa/products/catSearch, last access: 25 January 2021.

Swadley, S. D., Poe, G. A., Bell, W., Ye Hong, Kunkee, D. B., McDermid, I. S., and Leblanc, T. (2008). Analysis and characterization of the SSMIS upper atmosphere sounding channel measurements. *IEEE Transactions on Geoscience and Remote Sensing*, **46**(4), 962–983. https://doi.org/10.1109/TGRS.2008.916980

Tribbia, J. J, & Madden, R. A. (1988). Projection of time-mean geopotential heights onto normal Hough modes, *Meteorology and Atmospheric Physics*, **38**, 9–21. https://doi.org/10.1007/BF01029943

Watanabe, S., K. Hamilton, T. Sakazaki, and M. Nakano, (2022) First detection of the Pekeris internal global atmospheric resonance: Evidence from the 2022 Tonga eruption from global reanalysis data. *Journal of the Atmospheric Sciences*, **79**, 3027–3043. https://doi.org/10.1175/JAS-D-22-0078.1

Watanabe, S. & Miyahara, S. (2009). Quantification of the gravity wave forcing of the migrating diurnal tide in a gravity wave-resolving general circulation model. *Journal of Geophysical Research Atmosphere*, **114**, D07110. https://doi.org/10.1029/2008JD011218

Weber, R. O. & Madden, R. A. (1993). Evidence of traveling external Rossby waves in the ECMWF analyses. *Journal of the Atmospheric Sciences*, **50**(17), 2994–3007. https://doi.org/10.1175/1520-0469(1993)050%3C2994:EOTERW%3E2.0.CO;2

Yasui, R., Sato, K., & Miyoshi, Y. (2018). The momentum budget in the stratosphere, mesosphere, and lower thermosphere. Part 2: the in situ generation of gravity waves. *Journal of the Atmospheric Sciences*, **75**(10), 3635–3651. https://doi.org/10.1175/JAS-D-17-0337.1

Yasui, R., Sato, K., & Miyoshi, Y. (2021). Roles of Rossby waves, Rossby waves, Rossby-gravity waves, and gravity waves generated in the middle atmosphere for interhemispheric coupling. *Journal of the Atmospheric Sciences*, **78**(12), 3867–3888. https://doi.org/10.1175/JAS-D-21-0045.1

Yamazaki, Y., Matthias, V., and Miyoshi, Y. (2021). Quasi-4-day wave: atmospheric manifestation of the first symmetric Rossby normal mode of zonal wavenumber 2. *Journal of Geophysical Research*, **126**(13), e2021JD034855, https://doi.org/10.1029/2021JD034855

List of Figures

Fig. 1. (a) Theoretical horizontal structure of the $s = 1$ RG mode. The color indicates the geopotential component and the green arrows indicate the horizontal wind vectors. (b) Hough function (theoretical meridional structure) of the $s = 1$ RG mode. The solid curve shows the geopotential component, dashed curve shows the zonal wind component, and dash-dotted curve shows the meridional wind component.

Fig. 2. Power spectra for the westward $s = 1$ GPH fluctuations (black curve) and those removing the DW1 component (red curve). Plotted are the averages for $z = 45$–55 km at $30°$S. A 5-point running mean is applied. The green solid line shows a 1.3-day period corresponding to the spectral peak. The dashed green lines show the cut-off frequencies of the Ormsby bandpass filter.

Fig. 3. Filter characteristics of the Ormsby filter used in this study. (a) Characteristic function and (b) transfer function of the filter. The green solid line is the center of the passband, and the green dashed lines are the cut-off frequencies (i.e., $2\pi/1.11$ rad day^{-1} and $2\pi/1.58$ rad day^{-1}).

Fig. 4. Zonal wavenumber – frequency power spectra for GPH fluctuations at $30°$S for (a) $z = 30$, (b) 50, (c) 65, and (d) 80 km. A 5-point running mean is applied for the frequency direction. The black curve in each panel shows the dispersion curve of the RG normal modes, and the black circle shows the location of the westward $s = 1$ RG mode ($s = 1$ and a period of 1.18 days).

Fig. 5. Time-latitude sections of the climatology of the GPH amplitude of RG1 at (a) $z = 30$, (b) 50, (c) 65, and (d) 80 km. A 15-day running mean is applied. The contour intervals are (a) 0.375 m, (b) 1.25 m, (c) 2 m, and (d) 4 m. In the bottom right panel, the solid curve represents the latitudinal profile of the Hough function of the $s = 1$ RG mode.

Fig. 6. Time-latitude sections of the RG1 GPH amplitude for 16 years at $z = 30, 50, 65$, and $80\ \mathrm{km}$ from the top. Tick marks show the 1st of January of each year.

Fig. 7. Latitude-height sections of the normalized GPH amplitude $\sqrt{\overline{\mathrm{GPH}'^2}} \times e^{-\kappa z/H}$ climatology in December to January, in March to April, in June to July, and in September to October, from the left. The contour interval is $0.075\ \mathrm{m}$.

Fig. 8. A time-height section of the normalized GPH amplitude $\sqrt{\overline{\mathrm{GPH}'^2}} \times e^{-\kappa z/H}$ over 16 years at $30°\mathrm{N}$.

Fig. 9. A time-height section of the normalized GPH amplitude $\sqrt{\overline{\mathrm{GPH}'^2}} \times e^{-\kappa z/H}$ (color) and zonal mean zonal wind (contour) from November 20 to December 15 in 2009 at $30°\mathrm{N}$. A 3-day running mean is applied. The contour interval is 5 m/s.

Fig. 10. Latitude-height sections of the normalized GPH amplitude $\sqrt{\overline{\mathrm{GPH}'^2}} \times e^{-\kappa z/H}$ every 3 days 00UTC on November 28 to 00UTC on December 7, 2009. The contour interval is 0.2 m.

Fig. 11. Longitude-latitude sections of the RG1 GPH component and the RG1 horizontal wind vectors at $z = 80\ \mathrm{km}$ every 6 hours over the period of 00UTC on December 4 to 06 UTC on December 5, 2009. The colors and green arrows indicate the GPH components and horizontal wind vectors, respectively. The contour interval is $10\ \mathrm{m}$ and unit vector shows a magnitude of $10\ \mathrm{ms}^{-1}$.

Fig. 12. Longitude-height sections of the normalized GPH component $\mathrm{GPH}' \times e^{-\kappa z/H}$ at $30°\mathrm{N}$ and $30°\mathrm{S}$ on December 4, 2009, 00UTC.

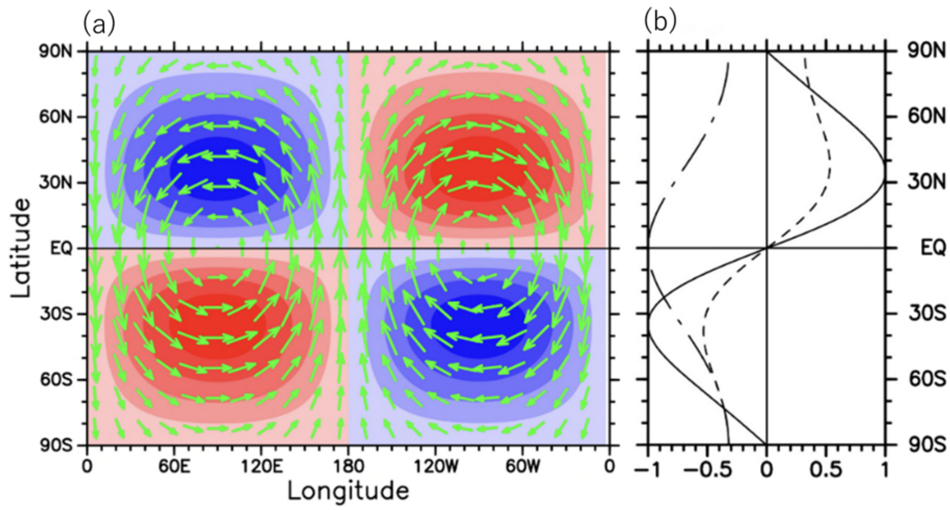

Fig. 1. (a) Theoretical horizontal structure of the *s*=1 RG mode. The color indicates the geopotential component and the green arrows indicate the horizontal wind vectors. (b) Hough function (theoretical meridional structure) of the *s*=1 RG mode. The solid curve shows the geopotential component, dashed curve shows the zonal wind component, and dash-dotted curve shows the meridional wind component.

428x226mm (57 x 57 DPI)

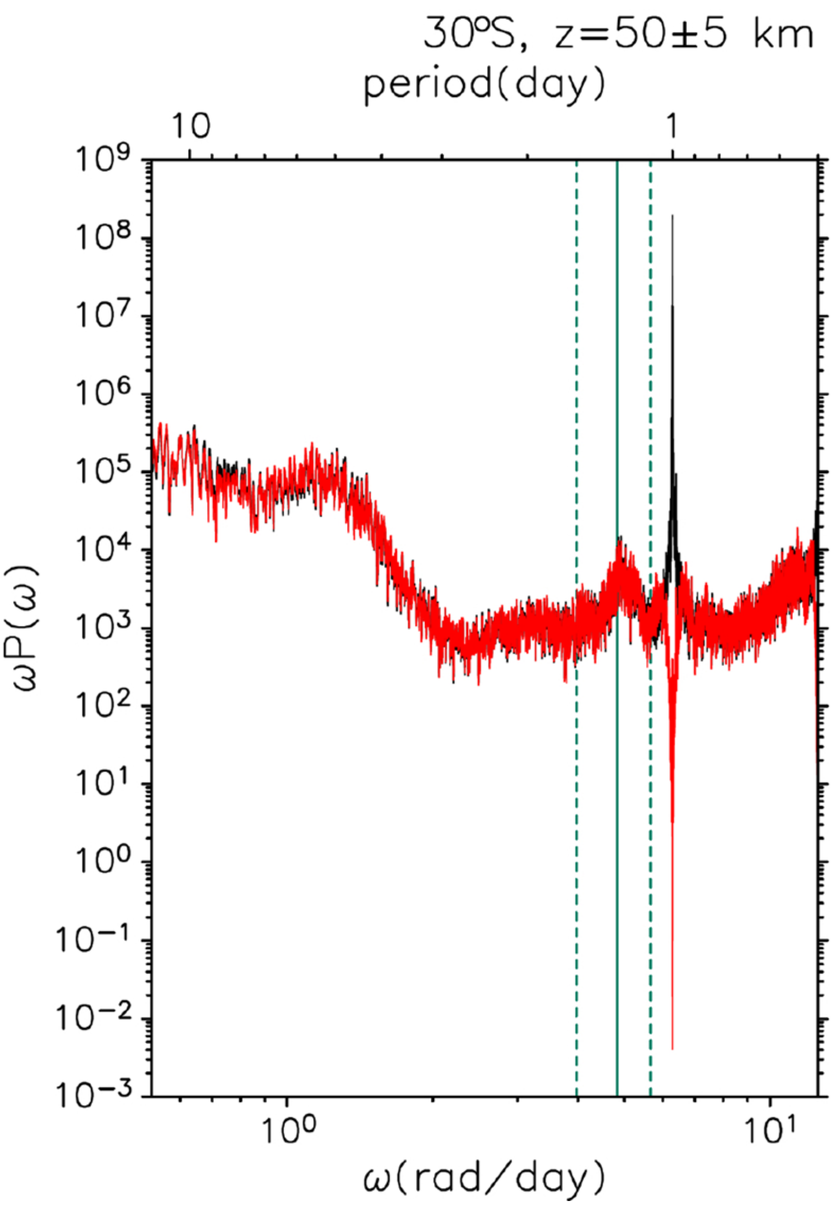

Fig. 2. Power spectra for the westward s=1 GPH fluctuations (black curve) and those removing the DW1 component (red curve). Plotted are the averages for z=45–55 km at 30°S. A 5-point running mean is applied. The green solid line shows a 1.3-day period corresponding to the spectral peak. The dashed green lines show the cut-off frequencies of the Ormsby bandpass filter.

354x503mm (57 x 57 DPI)

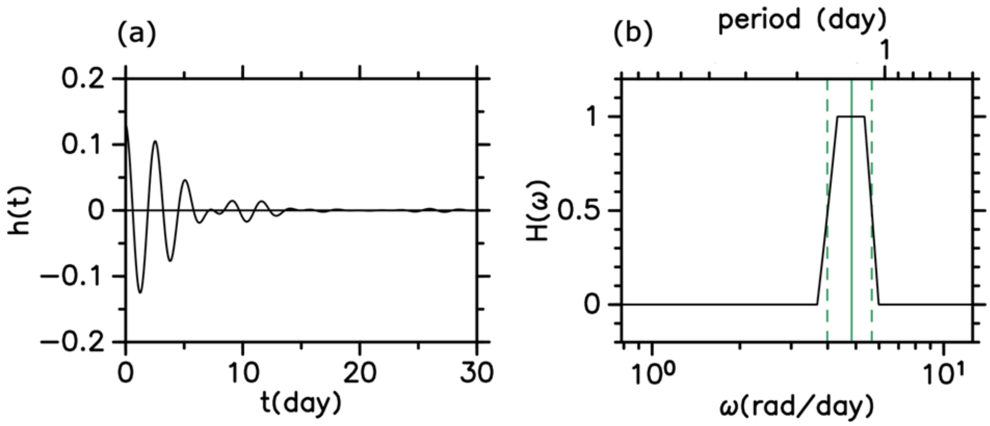

Fig. 3. Filter characteristics of the Ormsby filter used in this study. (a) Characteristic function and (b) transfer function of the filter. The green solid line is the center of the passband, and the green dashed lines are the cut-off frequencies (i.e., $2\pi/1.11$ rad day^{-1} and $2\pi/1.58$ rad day^{-1}).

428x184mm (57 x 57 DPI)

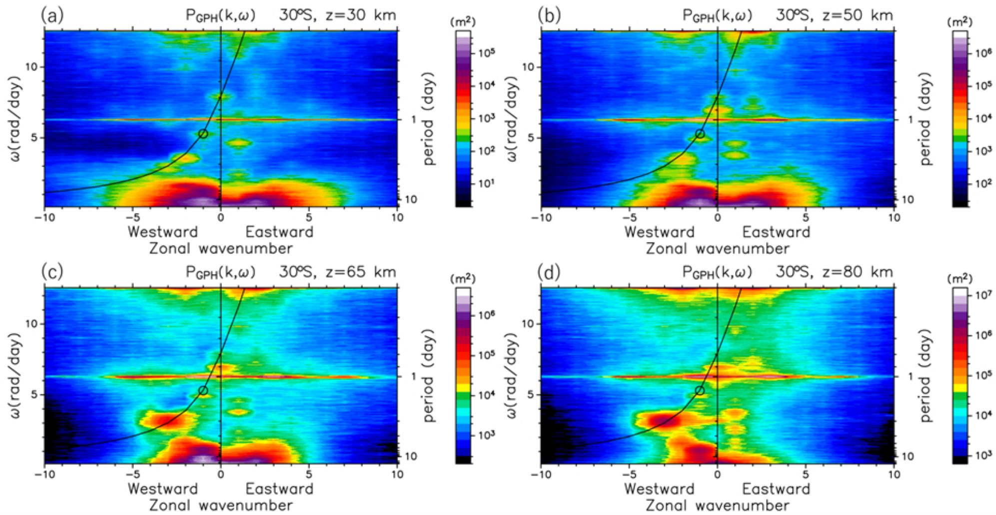

Fig. 4. Zonal wavenumber – frequency power spectra for GPH fluctuations at 30°S for (a) *z*=30,(b) 50,(c) 65, and (d) 80 km. A 5-point running mean is applied for the frequency direction. The black curve in each panel shows the dispersion curve of the RG normal modes, and the black circle shows the location of the westward *s*=1 RG mode (*s*=1 and a period of 1.18 days).

430x220mm (57 x 57 DPI)

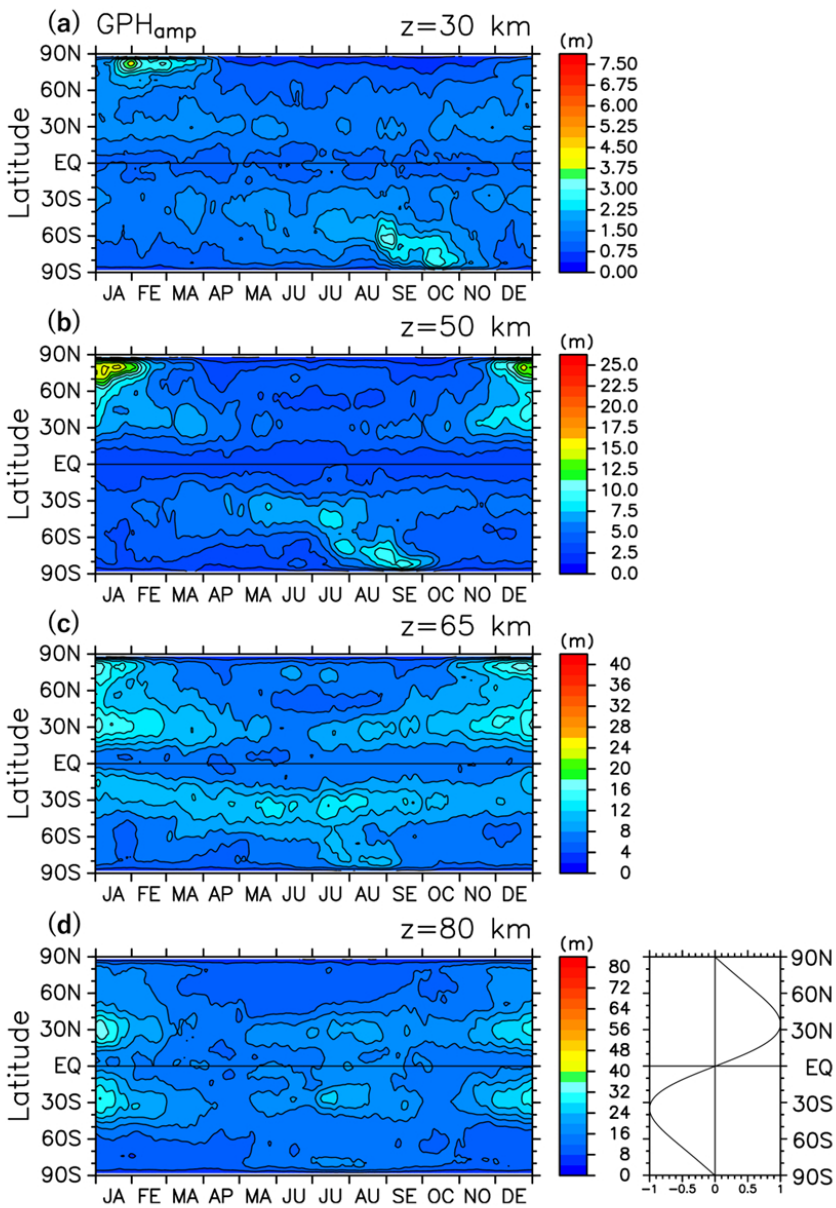

Fig. 5. Time-latitude sections of the climatology of the GPH amplitude of RG1 at (a) z=30,(b) 50,(c) 65, and (d) 80 km. A 15-day running mean is applied. The contour intervals are (a) 0.375 m,(b)1.25 m,(c) 2 m, and (d) 4 m. In the bottom right panel, the solid curve represents the latitudinal profile of the Hough function of the s=1 RG mode.

363x520mm (57 x 57 DPI)

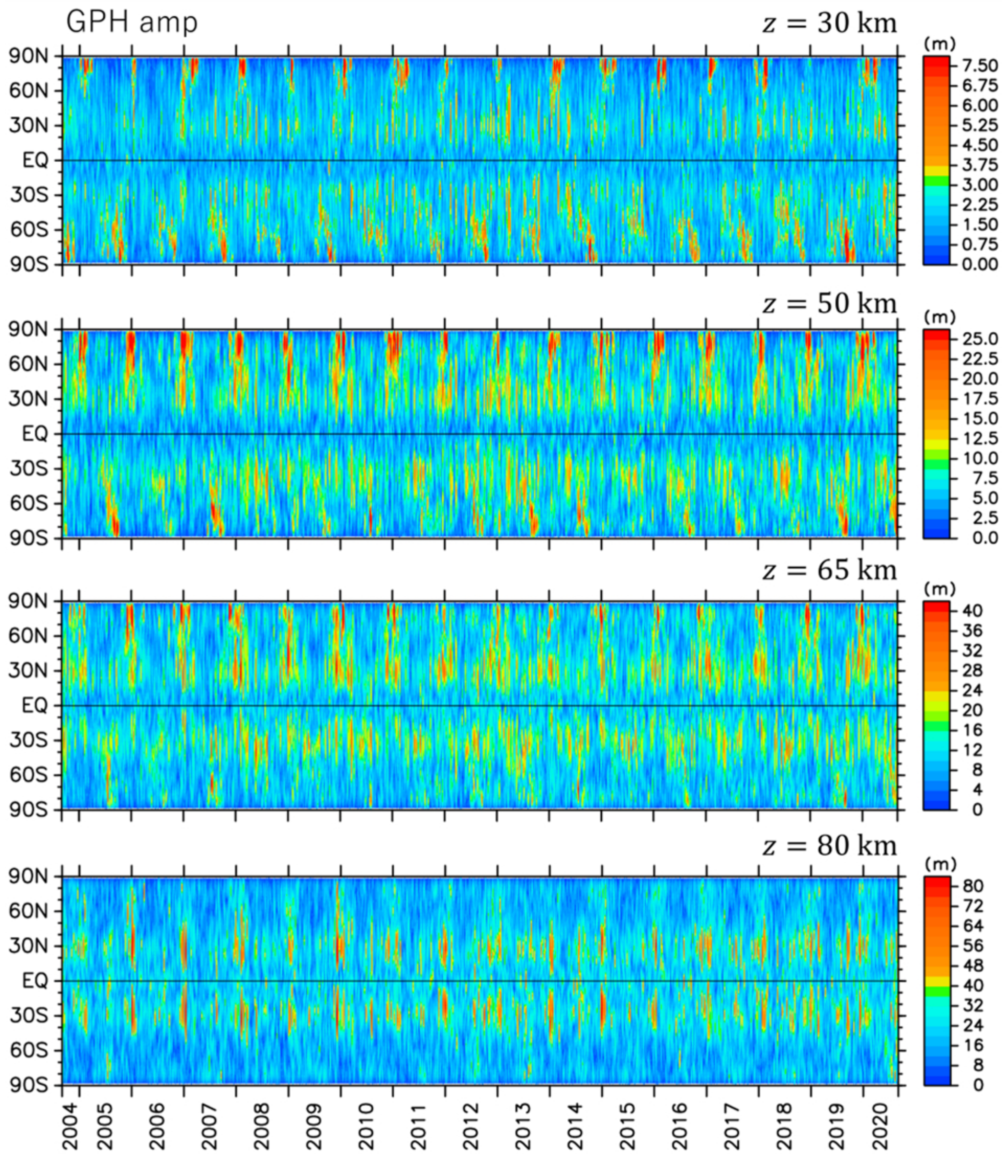

Fig. 6. Time-latitude sections of the RG1 GPH amplitude for 16 years at z=30,50,65, and 80 km from the top. Tick marks show the 1st of January of each year.

426x492mm (57 x 57 DPI)

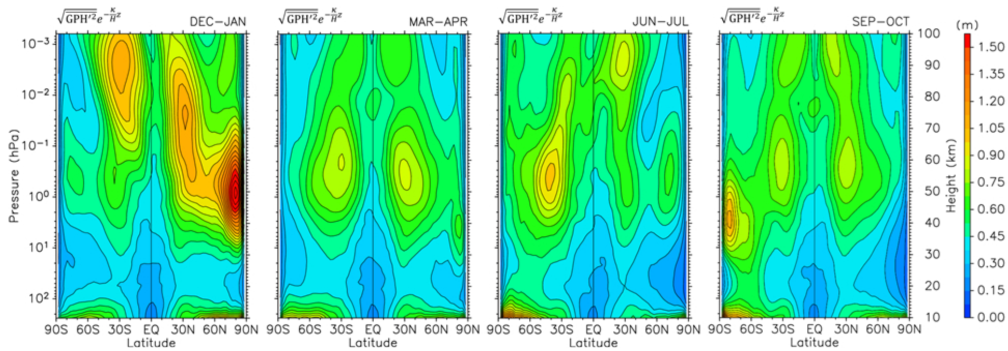

Fig. 7. Latitude-height sections of the normalized GPH amplitude climatology in December to January, in March to April, in June to July, and in September to October, from the left. The contour interval is 0.075 m.

429x147mm (57 x 57 DPI)

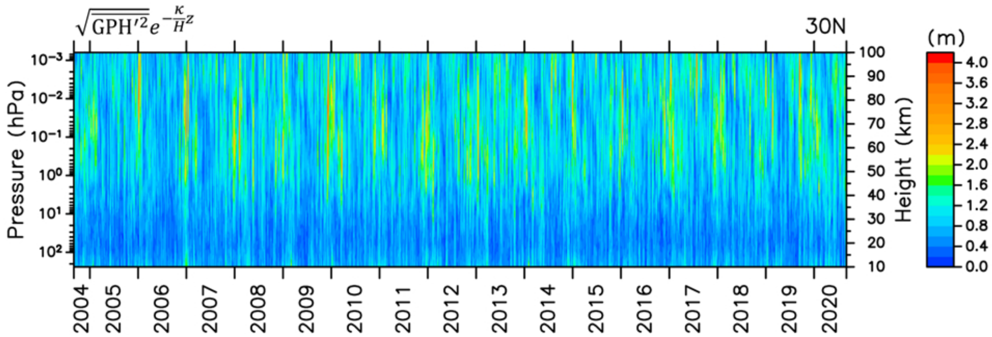

Fig. 8. A time-height section of the normalized GPH amplitude over 16 years at 30°N.

429x143mm (57 x 57 DPI)

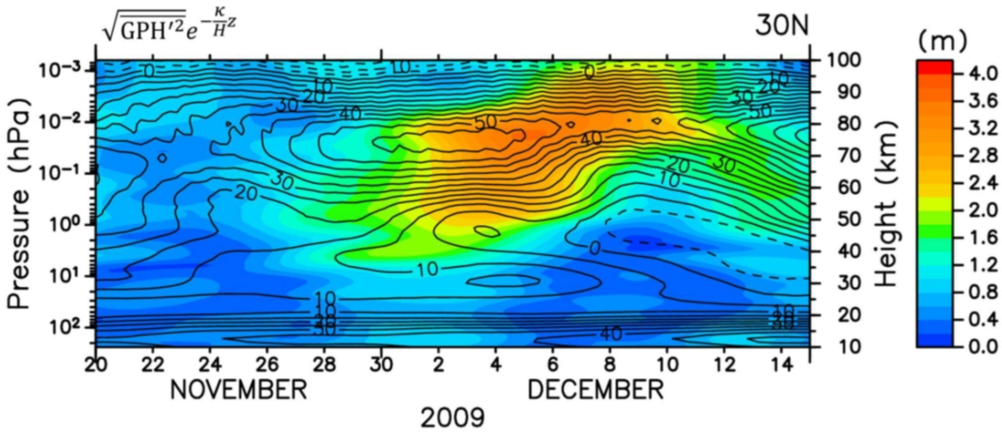

Fig. 9. A time-height section of the normalozed GPH amplitude (color) and zonal mean zonal wind (contour) from November 20 to December 15 in 2009 at 30°N. A 3-day running mean is applied. The contour interval is 5 ms^{-1}.

430x186mm (73 x 73 DPI)

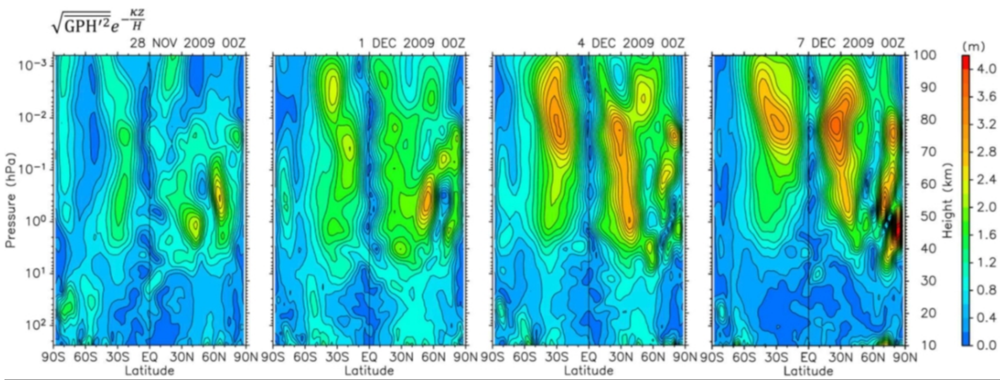

Fig. 10. Latitude-height sections of the normalized GPH amplitude every 3 days 00UTC on November 28 to December 7, 2009. The contour interval is 0.2 m

430x161mm (73 x 73 DPI)

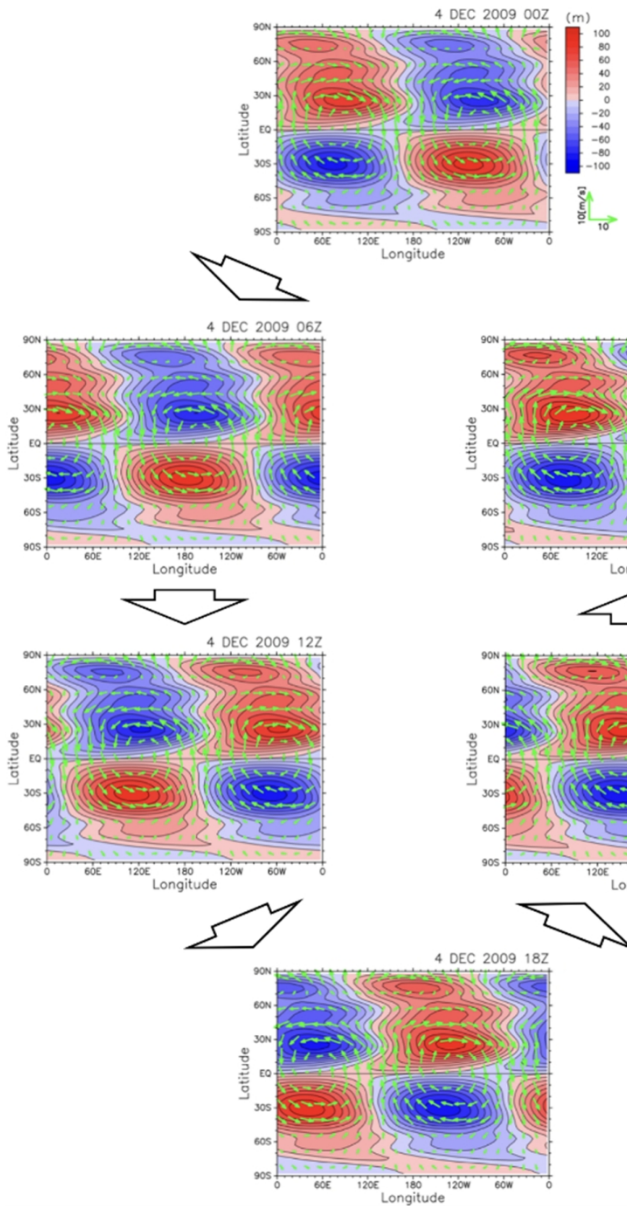

Fig. 11. Longitude-latitude sections of the RG1 GPH component and the RG1 horizontal wind vectors at *z*=80 km every 6 hours over the period of 00UTC on December 4 to 06 UTC on December 5, 2009. The colors and green arrows indicate the GPH components and horizontal wind vectors, respectively. The contour interval is 10 m and unit vector shows a magnitude of 10 ms^{-1}.

351x534mm (87 x 87 DPI)

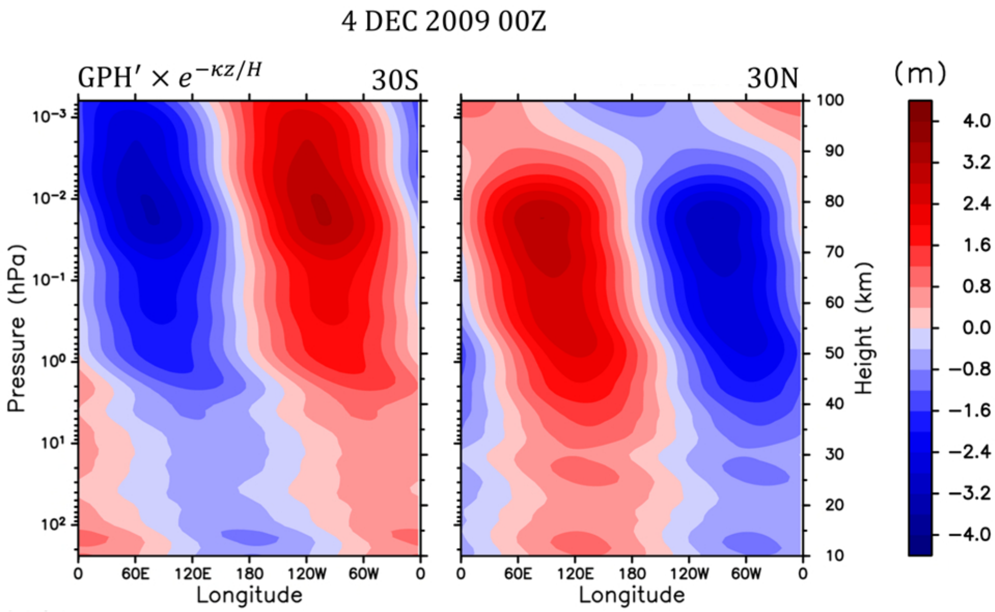

Fig. 12. Longitude-height sections of the normalized GPH component at 30°N and 30°S on December 4, 2009, 00UTC.

429x260mm (57 x 57 DPI)